



Continuum and magnetic dipole absorption of the water vapor–oxygen mixtures from 0.3 to 3.6 THz

V.B. Podobedov^{a,*}, D.F. Plusquellic^a, K.M. Siegrist^a, G.T. Fraser^a, Q. Ma^b, R.H. Tipping^c

^aOptical Technology Division, National Institute of Standards and Technology, 100 Bureau Drive, Gaithersburg, MD 20899, USA

^bNASA/Goddard Institute for Space Studies, Department of Applied Physics and Applied Mathematics, Columbia University, 2880 Broadway, New York, NY 10025, USA

^cDepartment of Physics and Astronomy, University of Alabama, Tuscaloosa, AL 35487, USA

ARTICLE INFO

Article history:

Received 15 January 2008

In revised form 21 February 2008

Available online 18 March 2008

Keywords:

Continuum

IR

THz

Oxygen

Water vapor

Atmosphere

ABSTRACT

The measurement of absorbance in water vapor–oxygen mixtures is reported for the far-IR region from 10 to 120 cm^{−1} (0.3–3.6 THz). The experiments were performed in a temperature-stabilized multipass absorption cell coupled to a far-infrared Fourier transform spectrometer with a liquid-He-cooled bolometer detector. The absorbance components due to both the H₂O–O₂ continuum and the oxygen magnetic dipole discrete lines have been measured in the temperature range from 294 to 333 K with a spectral resolution of 0.03 to 0.07 cm^{−1}. In the range up to 2.5 THz, the H₂O–O₂ continuum demonstrates a nearly quadratic dependence of absorbance on frequency, while in the 3.43 THz window deviation from this dependence was detected. The series of rotational lines associated with magnetic dipole transitions was measured in pure oxygen. In the mixture of 1.36 kPa of water vapor and 79.2 kPa of oxygen, a comparable contribution from continuum and discrete lines associated with magnetic dipole transitions of O₂ was observed. The absorption coefficient of 0.066 (dB/km)/(kPa THz)² and its temperature exponent of 4.7 were measured for the H₂O–O₂ continuum. Experimental continua data compared to theoretically predicted values exhibit good agreement. The modeling of the resonant water vapor spectrum was performed using a Van Vleck–Weisskopf lineshape with a 215 cm^{−1} far-wing cut-off and the HITRAN2004 database.

Published by Elsevier Inc.

1. Introduction

The water vapor continua, both the self-continuum (H₂O–H₂O) and the foreign continua (H₂O–N₂ and H₂O–O₂), play important roles for many atmospheric applications, especially in dry air environments [1]. There has been a great deal of experimental [2–6] and theoretical work [7–12], mainly on the infrared windows between the strong vibration-rotational bands of water vapor. Some work has also been done at microwave and millimeter wavelengths [13–19], but only recently has work been done to extend the measurements and theoretical calculations into the THz region [20,21]. In this region, the number and strength of the pure rotational H₂O lines increase and accurate measurements of the underlying baseline continuum become difficult. Also, the measurements have to be limited to the narrow windows between individual lines. In a previous paper [21], we have presented experimental results and theoretically calculated values for temperatures between 293 and 333 K for the self- and the H₂O–N₂ foreign continua. In the present paper, we extend these results to the H₂O–O₂ continuum

where the measurements are more difficult for two reasons: (1) the magnitude of the absorbance in H₂O–O₂ is smaller than that in H₂O–N₂ because of the weaker interaction potential during collisions that is responsible for the continuum absorption; and (2) the O₂ molecule has magnetic dipole transitions in this region that have to be accounted for as additional absorbing components in the measured spectra [22]. Because of the latter effect, we have also made measurements of the magnetic dipole lines in pure O₂.

The paper is organized as follows. In Section 2, we present a brief review of the theory previously used to calculate the absorption coefficient and its temperature dependence up to 450 GHz for H₂O–N₂ [15]. We then give the details of the experimental measurements in Section 3. In Section 4, we present the results and comparisons between theory and experiment. Finally, in Section 5, we discuss the conclusions drawn from this work.

2. Theory

To apply the theory used previously for calculating the millimeter-wave H₂O–N₂ continuum [15] to the calculation of the H₂O–O₂ continuum in the THz region, we briefly outline the basic formalism. For the binary collision approximation valid in atmospheric

* Corresponding author. Fax: +1 301 869 5700.

E-mail address: Vyacheslav.Podobedov@nist.gov (V.B. Podobedov).

environments, the absorption coefficient $\alpha(\omega)$ at the frequency ω (in cm^{-1}) can be expressed as

$$\alpha(\omega) = \frac{4\pi^2}{3\hbar c} n_{\text{pair}} \omega \tanh(\beta\hbar\omega/2) [F(\omega) + F(-\omega)], \quad (1)$$

where n_{pair} is the pair number density. The spectral density $F(\omega)$ is given by

$$F(\omega) = -\frac{1}{\pi} \text{Im Tr}_r \left\{ \rho_{\text{iso}} \text{Tr}_{ab} \left[\tilde{\mu}^\dagger \sqrt{\rho_a \rho_b} \frac{1}{\omega - \mathcal{L}} \sqrt{\rho_a \rho_b} \tilde{\mu} \right] \right\}, \quad (2)$$

where the whole trace is divided into a trace over the translational degree denoted by Tr_r and a trace over internal degrees denoted by Tr_{ab} . In the above expression, $\tilde{\mu}$ is the dipole operator of H_2O and \mathcal{L} is the Liouville operator associated with the total Hamiltonian of the $\text{H}_2\text{O}-\text{O}_2$ pair. With the Lanczos algorithm, one can define the starting vector $|v\rangle = \sqrt{\rho_a \rho_b} \tilde{\mu}$ in the Liouville space and write the inner trace of $F(\omega)$ in terms of a continued fraction,

$$\text{Tr}_{ab} \left[\tilde{\mu}^\dagger \sqrt{\rho_a \rho_b} \frac{1}{\omega - \mathcal{L}} \sqrt{\rho_a \rho_b} \tilde{\mu} \right] = \langle v | v \rangle \frac{1}{\omega - \alpha_1 - \frac{\beta_2^2}{\omega - \alpha_2 - \frac{\beta_3^2}{\omega - \alpha_3 - \dots}}}, \quad (3)$$

where $\alpha_1, \beta_2, \alpha_2, \beta_3$, and α_3 are parameters that can be derived from the matrix elements $\langle v | \mathcal{L} | v \rangle, \langle v | \mathcal{L}^2 | v \rangle, \dots$, and $\langle v | \mathcal{L}^5 | v \rangle$.

At this stage, the introduction of the coordinate representation plays a crucial role because with the standard method, to evaluate $\langle v | \mathcal{L}^n | v \rangle$ with $n \geq 2$ is intractable. Instead of choosing the internal states, one can select the orientations of the pair of molecules as the basis set in Hilbert space. By introducing this coordinate representation, the matrix elements $\langle v | \mathcal{L}^n | v \rangle$ becomes 9-dimensional integrations and the integrands are ordinary functions. A Monte Carlo algorithm (VEGAS) [23] is used to carry out the integrations. By taking approximately 10^7 random selections of a set of the 9 angular variables, this method yields convergent results.

For the tetrahertz windows of interest in the present study, whose center frequencies are not outside of the rotational band of H_2O , the method described above is not directly applicable. However, in comparison with the strongest lines of the H_2O band, the frequencies of these windows are still low. As a result, one can modify the original theoretical method and use it to calculate the THz continuum. Within this modified theory, the starting vector $|v\rangle$ has been replaced by a modified one $|v\rangle_{\text{sub}}$ for a specified window of interest. In the original starting vector, the dipole operator spans all possible $|i j^*\rangle$ in the Liouville space, where i and j stand for the initial and final states of all the H_2O lines. Meanwhile, for the modified starting vector, the dipole operator spans only those $|i j^*\rangle$ in a Liouville sub-space consisting of lines whose frequencies are higher than the window frequency. With respect to other $|i j^*\rangle$, whose transition frequencies are lower than the window frequencies, they are treated as local lines. This is the main difference between the original and the modified formalisms.

Next, we would like to present a detailed description of potential models used in the present and the previous studies. Because both O_2 and N_2 are linear molecules, the form of the potential models for $\text{H}_2\text{O}-\text{O}_2$ and $\text{H}_2\text{O}-\text{N}_2$ is the same. The only differences are in the molecular and potential parameters. Generally speaking, one expects that except at very short ranges, the interaction between H_2O and O_2 is significantly weaker than that for H_2O and N_2 because the dipole–quadrupole interaction is the leading long-range interaction and the magnitude of the quadrupole moment of O_2 is approximately a factor of 4 smaller than that of N_2 . Consequently the $\text{H}_2\text{O}-\text{O}_2$ continuum is weaker than the $\text{H}_2\text{O}-\text{N}_2$ continuum.

In the present study, we assume

$$V(r, \Omega_a, \Omega_b) = V_{dq}(r, \Omega_a, \Omega_b) + V_{qq}(r, \Omega_a, \Omega_b) + V_{\text{ind}}(r, \Omega_a, \Omega_b) + V_{\text{atom}}(r, \Omega_a, \Omega_b), \quad (4)$$

where the first two components are the well known dipole–quadrupole and the quadrupole–quadrupole interactions between the H_2O and O_2 molecules. Values of the dipole and quadrupole moments of H_2O used in the calculations are $\mu = 1.8546$ D, $\theta_{bb} = -0.13$ D Å, $\theta_{cc} = -2.50$ D Å, and $\theta_{aa} = 2.63$ D Å [24]. Meanwhile, the quadrupole moments of O_2 and N_2 are -0.39 D Å and -1.466 D Å, respectively.

The induced interaction $V_{\text{ind}}(r, \Omega_a, \Omega_b)$ results from a mechanism that the dipole and quadrupole of H_2O yield an electric field at O_2 . This acts on the polarizability tensor α of O_2 and the latter acts back on H_2O . In terms of the orientation variables α, β , and γ for H_2O and the orientation variables θ and φ for O_2 , a detailed expression for $V_{\text{ind}}(r, \Omega_a, \Omega_b)$ is given in the appendix. The isotropic and anisotropic parts of the polarizability of O_2 are $\alpha = 10.87$ a.u. and $\gamma = 7.30$ a.u., respectively, and those for N_2 are 11.74 a.u. and 4.75 a.u., respectively [25,26].

Finally, the atom–atom interaction term is given by

$$V_{\text{atom}}(r, \Omega_a, \Omega_b) = \sum_{i \in a} \sum_{j \in b} 4\epsilon_{ij} \left\{ \left(\frac{\sigma_{ij}}{r_{ij}} \right)^{12} - \left(\frac{\sigma_{ij}}{r_{ij}} \right)^6 \right\}, \quad (5)$$

where the indices i and j run over the atoms of H_2O and O_2 , respectively, r_{ij} is the distance between the atom i of H_2O and the atom j of O_2 , ϵ_{ij} and σ_{ij} are Lennard–Jones (L–J) parameters. The parameters for V_{atom} used in the calculations are listed in Table 1.

It is worth mentioning that $V(r, \Omega_a, \Omega_b)$ contains an isotropic component because V_{atom} consists of the isotropic and anisotropic components. The effective L–J parameters derived from the potential models of $\text{H}_2\text{O}-\text{O}_2$ and $\text{H}_2\text{O}-\text{N}_2$ given above are $\sigma_{\text{eff}} = 3.66$ Å, $\epsilon_{\text{eff}} = 159$ K, and $\sigma_{\text{eff}} = 3.64$ Å, $\epsilon_{\text{eff}} = 131$ K, respectively.

Based on this potential model, one can calculate the matrix elements $\text{sub} \langle v | \mathcal{L}^n | v \rangle_{\text{sub}}$ and the corresponding parameters $\alpha_1, \beta_2, \alpha_2, \beta_3$, and α_3 appearing in the continued fraction. Then one can obtain the continuum for a specified window. We note that the continuum and the local line contributions in a given window are intertwined. Therefore, it is necessary to specify how the local contributions are calculated when presenting theoretical continuum results. Within the present modified Lanczos method, those $|i j^*\rangle$ whose transition frequencies are lower than the frequency of the window of interest are considered to be the local lines. However, H_2O lines whose frequencies are somewhat higher than the window frequency must also be treated as local lines because the sharp absorption structures resulting from them are missing from the smooth Lanczos results. Unfortunately, there is no method to determine exactly how far away from the window center (i.e., the upper-frequency limits ν_{cut}) as a limit for those lines must be included. With the current method, the ranges for the upper-frequency cut-off ν_{cut} for each of the windows are estimated, as those cannot be determined exactly. Consequently these upper-frequency cut-offs become adjustable parameters. It is worth mentioning that the upper-frequency cut-offs discussed here differ from those introduced previously when calculating measured continuum results. This adjustment procedure has been discussed in our paper [21] for $\text{H}_2\text{O}-\text{N}_2$.

Table 1
Potential parameters used for V_{atom}

$\text{H}_2\text{O}-\text{O}_2$			$\text{H}_2\text{O}-\text{N}_2$		
Atom pair	σ (Å)	ϵ (K)	Atom pair	σ (Å)	ϵ (K)
H–O	2.95	40	H–N	3.00	28
O–O	3.10	65	O–N	3.15	52

Finally, two optimization procedures have been taken. The first one optimizes the half-width ratio between O_2 and air broadening. The experimental continuum is sensitive to this ratio because it is given by the small difference between two large values (i.e., the measured raw result and the calculated local line contributions), and the local line contributions depend sensitively on the O_2 broadened half-widths. The theoretical calculated continuum is less sensitive to the O_2 broadened half-widths because the magnitudes involved are comparable. We have used these different sensitivities to select the optimized half-width ratio as 0.61. After presenting the experimental values derived from the selection of $O_2/\text{air} = 0.61$, the second procedure is carried out in which the ν_{cut} are treated as adjustable parameters to optimize the theoretical results to get the best agreement with the experimental continuum values. Consequently, the current theoretical continuum results are not truly *ab initio*.

3. Experimental measurements

The measurements were performed in a multipass cell previously described in Ref. [20]. The cell was coupled to a polarizing (Martin–Puplett) interferometric spectrometer with a long-pass filter optimized for the maximum signal-to-noise ratio in the range below 125 cm^{-1} . Measurements were made with spectral resolution of $0.03\text{--}0.06\text{ cm}^{-1}$. A 60-mm input aperture and $f/2$ optics used in the cell as well as coupling optics were chosen to provide acceptable diffraction losses at the lowest operational frequency. The variable cell pathlength for this experiment was set to 40 passes, the equivalent of about 24 m. The precise value of 23.3 m was defined from a calibration procedure described previously [20]. The whole cell was surrounded with a thermo-insulation cover and was equipped with silicon rubber heaters controlled by a temperature stabilization unit. For temperatures between 20 and 70°C , the uncertainty in the measured temperature did not exceed 0.2°C [21]. After preheating the cell filled with gaseous He at a rate of about 5°C/h and temperature stabilizing, it was evacuated below 0.1 Pa. Then the cell was consequently filled with an $H_2O\text{--}O_2$ mixture. Triply distilled water and high-purity oxygen (99.9999% purity) were mixed at this step. The pressure of each component was measured with two capacitance diaphragm gauges with an uncertainty of about 0.1 Pa for water vapor and about 10 Pa for oxygen. Each measurement session normally included three spectra of which the first and the last spectra used as references were obtained from the cell filled with nitrogen. As compared to the evacuated cell, the use of nitrogen in this case provided smaller error caused by a variation of a standing wave reflection in the reference spectra. Together with other measurements taken, this allowed us to estimate the experimental uncertainty of the measured absorbance as ± 0.006 . In this paper, the absorbance, A , is expressed in logarithmic units using the base 10 so that $A = \log_{10}(1/T)$. Where possible, the second absorbance scale in the frequently used units of dB/km, is also presented. The absorbance data in this work may be converted into a corresponding absorption coefficient so that the absorbance of $A = 1$ corresponds to an absorption coefficient of 429 dB/km.

4. Results and discussion

The $H_2O\text{--}O_2$ continuum absorption was measured in several windows centered at 22.5, 28.3, 34.3, 45.0, 50.3, 66.4, 70.1, 84.1 and 114.6 cm^{-1} , while the entire range from 10 to 120 cm^{-1} was available for measurements in pure oxygen. Note that the continuum absorbance may only be measured in the windows, i.e. near the minimum absorbance between the strong discrete water vapor lines. A similar procedure for continuum measurements in the $H_2O\text{--}N_2$ mixture was described in Ref. [21]. In this study, all the individual line parameters for water vapor in the THz range were

taken from the HITRAN2004 database and corrected for the difference between H_2O/O_2 and H_2O/air broadening efficiency as described below in Section 4.2. Using the input parameters including pressure, temperature, pathlength, lineshape, far-wing cut-off (100 cm^{-1}) and high-frequency cut-off (215 cm^{-1}), the local contributions of resonance water vapor spectra were modeled by the JB95 program [27]. A Van Vleck–Weisskopf lineshape [28] was assumed in the modeling. The line intensity was set to zero beyond the far-wing cut-off, and no contributions from lines beyond the high-frequency cut-off were included.

The total absorbance A of an $H_2O\text{--}O_2$ mixture has two components:

$$A(\nu, T) = A_R + A_C. \quad (6)$$

The components in Eq. (6) may be described as

$$A_R(\nu, T) = A_{H_2O} + A_{O_2}, \quad (7)$$

$$A_C(\nu, T) = A_{\text{self}}(P_{H_2O}^2) + A_{\text{foreign}}(P_{O_2}P_{H_2O}) + A_{\text{foreign}}(P_{O_2}^2), \quad (8)$$

where the index R denotes a resonance component from the rotational spectra of both water vapor and oxygen, and the index C indicates the continuum component. Notice that due to the different pressure dependence of the self- and foreign continua, the latter becomes dominant for the low water content of the mixture. A formula applicable to the absorption of the $H_2O\text{--}O_2$ mixture allows us to obtain the absorption coefficients and temperature exponents for water vapor and the foreign gas separately [21]:

$$A_C(\nu, T) = [K_{\text{self}}(\nu) \cdot (300/T)^{n_s} + K_{\text{for}}(\nu) \cdot (300/T)^{n_f}] \nu^2 L; \quad (9)$$

here $K_{\text{self}}(\nu)$ and $K_{\text{for}}(\nu)$ are the absorption coefficients, ν is the frequency, and L is the pathlength.

We note that the measured self-continuum term $A_{\text{self}}(P_{H_2O}^2)$ contains all contributions from different mechanisms and to determine their individual roles is beyond the scope of this study. However, it would be helpful to mention a recent theoretical study of water dimer absorption [29] where these authors have presented values of the self-continuum due to water dimers.

4.1. Self-continuum

Self-continuum data are needed to derive the foreign continuum from the raw absorbance data for $H_2O\text{--}O_2$ mixtures. It should be noted that compared to the $H_2O\text{--}N_2$ system, the role of the self-continuum in the definition of the $H_2O\text{--}O_2$ continuum is larger since the latter is expected to be smaller than in $H_2O\text{--}N_2$ mixtures having the same partial pressures of the mixture components. In the present study, we did not measure the H_2O self-continuum because these data were available from our previous work [21]. In the range up to 70.1 cm^{-1} , its value was defined using the parameters $K_{\text{self}} = 3.83$ and $n_s = 8.8$, viz. $3.83(300/T)^{8.8}$ (dB/km)/(kPa THz) 2 . Above the wavenumber of 70.1 cm^{-1} , where the quadratic dependence of the self-continuum on frequency is not justified, the self-continuum absorbance was taken directly from the experimental data by subtracting the resonance spectrum of water vapor predicted by the HITRAN2004 database. The complete set of self-continuum data used below is presented in Table 2.

4.2. $H_2O\text{--}O_2$ continuum

According to Eq. (8), the $H_2O\text{--}O_2$ continuum is defined as the difference between the total continuum absorbance of the $H_2O\text{--}O_2$ mixture and the self-continuum (Table 2). We neglect here the contribution of the collision-induced $O_2\text{--}O_2$ continuum because, for the selected partial pressures in the mixtures used, this contribution [30] is expected to be much smaller than the $H_2O\text{--}O_2$ continuum. The modeling of local contribution in the $H_2O\text{--}O_2$

Table 2

Experimental self-continuum absorbance (base 10) for water vapor at different temperatures (K)

Window center (cm ⁻¹)	T (K)				
	294	304	316	323	333
22.5	0.009	0.007	0.005	0.004	0.003
28.3	0.014	0.011	0.008	0.006	0.005
34.3	0.021	0.016	0.011	0.009	0.007
45.0	0.036	0.027	0.019	0.016	0.012
50.3	0.045	0.033	0.024	0.020	0.015
66.4	0.078	0.058	0.041	0.034	0.026
70.1	0.087	0.065	0.046	0.038	0.029
84.1	0.096	0.071	0.051	0.042	0.032
114.6	0.110	0.082	0.059	0.048	0.037

The water vapor pressure and absorbing path are 1.36 kPa and 23.3 m.

mixture was performed with the HITRAN2004 database using air broadening parameters. Therefore, the choice of both the O₂/air broadening ratio and the linewidth temperature dependence are very important for the determination of the H₂O–O₂ continuum. In a simplified approach, accounting for non-air broadening can be done by an artificial correction of the gas pressure used in the experiment that is related to the effective broadening ratio. For example, the N₂/air broadening ratio of 1.11 was normally applied in calculations of absorption in the mixture of water vapor with nitrogen [21]. Based on the percentage air composition (N₂ ≈ 78%, O₂ ≈ 21% and other ≈ 1%) the required O₂/air broadening ratio may be estimated between 0.586 and 0.634. It should be noted, however, that the average broadening ratio defined this way does not reflect the difference in the temperature dependence of the linewidth, which normally varies for different water vapor lines and foreign gases. Lack of experimental data in the THz range creates a problem for the accurate account of this behavior. Based on analysis of available data, we have chosen the O₂/air broadening ratio of 0.61. This value is close to some recent microwave data [31] and, as found below, provides the best match with the theoretically predicted continuum parameters. By using this ratio, any remaining differences in the temperature dependence of the linewidth between oxygen and air may increase the experimental uncertainty associated with our continuum measurements.

The absorbance data derived from experimental spectra are presented in Fig. 1a and b as a function of wavenumber and temperature. For the mixture composed of 1.36 kPa of water vapor and 79.2 kPa of oxygen, a nearly quadratic dependence of absorbance on frequency was observed similar to that reported in Ref. [21] and in some microwave studies for the H₂O–N₂ mixture [32,33]. In the range up to the 84.1 cm⁻¹ window, the deviation from a ν^2 -function does not exceed the experimental uncertainty, while in the highest window at 114.6 cm⁻¹, the observed deviation is a few times higher. This may be an indication of slower than ν^2 -rise of the continuum in this frequency region as predicted in Ref. [34]. In Fig. 2a and Table 3 we also present the theoretically calculated values for the H₂O–O₂ continuum. Notice that according to the present theory, a variation of the absorption coefficients and temperature exponents for individual windows is expected. Thus, an experimental absorbance may be affected by both measurement uncertainties and the location of each individual window. At this point, there are two choices for the treatment of the experimental data. The first choice is to consider the absorbance data at a single temperature over the frequency range and to fit to a ν^2 function. For the second choice, the individual windows are treated separately over the temperature range.

Assuming a ν^2 -dependence of continuum absorbance in the range up to 84.1 cm⁻¹, the fitting procedure was applied to this portion of data. The data fit to the ν^2 function presented in Fig. 1a will result in 5 temperature-dependent parameters, each

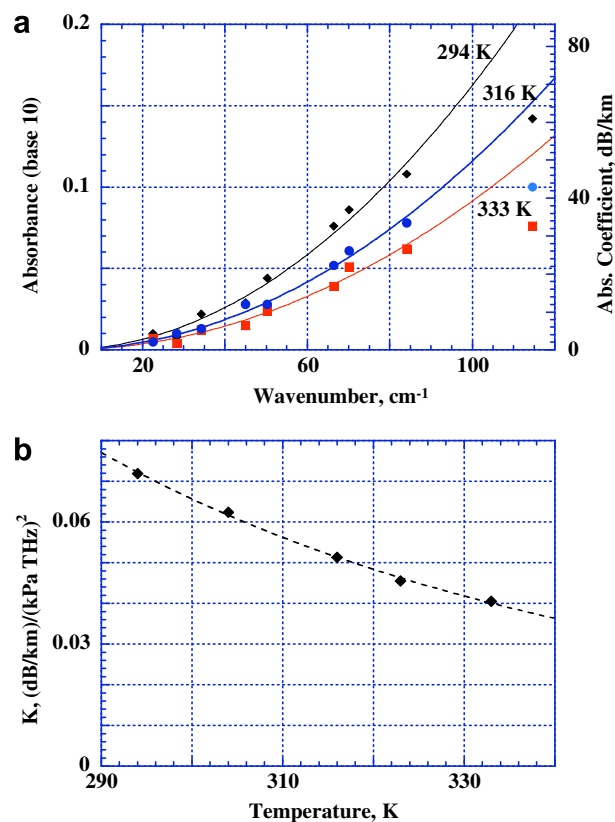


Fig. 1. (a) Continuum absorbance in the mixture of H₂O/O₂:1.36/79.2 kPa. Solid curves present the ν^2 -fit of data excluding the 114.6 cm⁻¹ window. (b) Temperature dependence of absorption coefficient for the H₂O/O₂ in (dB/km)/(kPa THz)² found from the fit in (a). The solid curve presents the second fit to the $(300/T)^n$ function as discussed in the text.

averaged over 8 windows during the quadratic fit. Thus if the ν^2 fit is appropriate, this procedure may provide a lower uncertainty in the results. The fitting formula used, $0.251K\nu^2$, accounts for both the absorption units and the component pressure in the H₂O/O₂ mixture so that the above 5 fitting parameters present the absorption coefficient, K , as a function of temperature. Then one can derive both the absorption coefficient (at $T = 300$ K) and temperature exponent, n_f , as presented in Fig. 1b. Here the data were fitted to the $K(300/T)^{n_f}$ function. Thus, within the range from 10 cm⁻¹ to 84.1 cm⁻¹, the absorption coefficient of 0.066 (dB/km)/(kPa THz)² and temperature exponent of 4.7 were found using both fits presented in Fig. 1a and b, respectively.

By considering each window individually, i.e. not assuming the ν^2 -dependence of continuum absorbance, both absorption coefficient and temperature exponent may be found for each window.

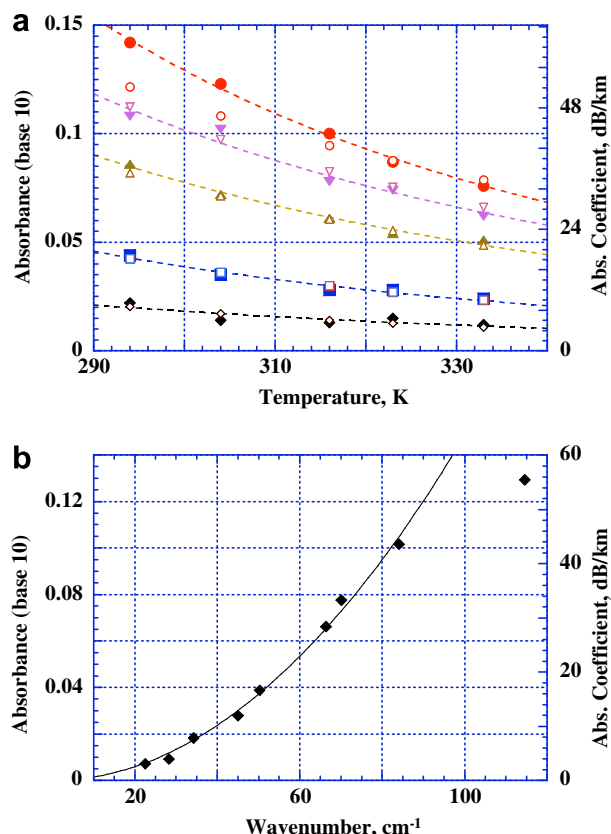


Fig. 2. (a) Absorbance data in several windows. For clarity, 5 of 9 available windows are represented: from top to bottom, 114.6, 84.1, 70.1, 50.3 and 34.3 cm^{-1} . Closed and open symbols present experimental and theoretical data, respectively. Solid curves are the fits of experimental data to the $(300/T)^{n_f}$ function. (b) Absorbance in the mixture of $\text{H}_2\text{O}/\text{O}_2$: 1.36/79.2 kPa at 300 K. The data were obtained from a fit to the data in (a). The solid curve presents the second fit to the ν^2 -function excluding the data in the 114.6 cm^{-1} window.

Table 3

Foreign continuum absorption coefficient, K_{for} , (dB/km)/(kPa THz^2) and temperature exponent, n_f , obtained from each transmittance window

Window center (cm^{-1})	K_{for}		n_f	
	Exp.	Theory	Exp.	Theory
22.5	0.063	0.061	5.6	4.87
28.3	0.051	0.052	4.6	5.31
34.3	0.068	0.069	4.5	5.07
45.0	0.061	0.060	4.3	4.84
50.3	0.068	0.067	5.0	4.79
66.4	0.066	0.060	5.8	4.07
70.1	0.070	0.068	4.5	4.20
84.1	0.064	0.065	4.5	4.25
114.6	0.044	0.038	5.1	3.48
<hr/>				
ν^2 -fitted (Exp.)	0.066(300/T) ^{4.7}		4.7	

The parameters given below the dashed line were determined from a global fit for the complete set of ν^2 -fitted curves (see Fig. 1a and b).

Fig. 2a presents the absorbance data in all nine available windows. Here the experimental data (closed symbols) in each window were fitted with the $A(300/T)^{n_f}$ function, where A and n_f would be absorbance and temperature exponent, respectively. Each fit involves five temperature points resulting in nine absorption coefficients and nine temperature exponents. The summary of continuum data found from individual windows is presented in Table 3 along with the theoretically calculated data. As noted above, the best match of experimental and theoretical data was observed at an O_2/air broad-

ening ratio of 0.61. The optimum ratio was chosen from data comparisons at 5 different O_2/air broadening ratios from 0.6 to 0.625. From the $A(300/T)^{n_f}$ fit of the experimental data, the parameter A obtained at $T = 300$ K may be then presented as a function of frequency as shown in Fig. 2b. It is interesting to notice that the nearly quadratic dependence of absorption coefficients over frequency is also observed similar to that demonstrated in Fig. 1a. At this point, the same value of absorption coefficient, $K = 0.066$ (dB/km)/(kPa THz^2), was obtained from the fit to the ν^2 -function.

4.3. Magnetic dipole absorption

Diatomic molecular oxygen ($^{16}\text{O}_2$) has no electric dipole moment, and thus the rotational spectrum due to this component is not observed in the absorption spectrum. However, due to the total electron spin of 1 in its electronic ground state, $^3\Sigma_g^-$, an oxygen molecule possesses a magnetic dipole moment. This moment causes relatively strong absorptions in both the microwave and THz regions that are sufficient for direct measurements [22]. Based on the usual magnetic dipole selection rules ($\Delta K = +2$, $\Delta J = +1$) and the rotational energy level diagram for molecular oxygen, the observed structure should consist of a series of relatively strong $\Delta J = 0$ peaks and weaker $\Delta J = \pm 1$ peaks.

The absorption spectrum of molecular oxygen in the microwave and submillimeter range was evaluated in a few studies [22,35]. Only limited data are available, however, for the absorption coefficients of the magnetic dipole oxygen lines in the THz region, in particular, above 85 cm^{-1} . The measurements of the absorbance for individual lines are usually affected by several factors, including weak signal strength, spectral resolution, line-mixing, and contributions from trace water vapor lines located close to a few oxygen lines. Some of these factors were reduced in the present study due to improved techniques, and a typical experimental absorption spectrum of pure oxygen is presented in Fig. 3 (solid curve). As expected from theory, a triplet-like structure was observed over the entire range from 10 cm^{-1} to 120 cm^{-1} . We note that frequencies and linewidths available for far-IR lines of molecular oxygen are currently known to smaller uncertainty than could be derived from our experimental data. Thus, most of our attention here will be given to the comparison of the line strength to that of the continuum absorption. The strength of individual oxygen lines may be directly estimated from this spectrum accounting for the pressure, path-length and the average linewidth (FWHM) of 0.113 cm^{-1} provided in this spectrum. This number includes both the self-width and the instrumental function. For example, the peak absorption coefficient of 21.9 dB/km for the strong line near 48.9 cm^{-1} is in good agreement with the data for the same line in Ref. [36] (10 dB/km at specified linewidth and pressure). For more accurate estimates of the strengths, data obtained with a high-spectral resolution technique will be needed.

In Fig. 3, the absorption spectrum of pure oxygen is presented together with a few other absorption components. As seen for the mixture presented in Fig. 3 (1.36 kPa of H_2O and 79.2 kPa of O_2), the discrete water vapor lines represented by the dotted curve significantly exceed the two other components, viz. the continuum and the magnetic dipole absorbance. Ignoring line-mixing, the magnetic dipole absorbance does not depend on the water vapor pressure. However, the first two components are proportional to this pressure; therefore a redistribution of the various absorptions is expected at smaller pressures of water vapor, and the relative importance of the magnetic dipole absorbance will increase as the humidity decreases. For dry atmospheric conditions, i.e. a very small concentration of water vapor, the total absorption will also be affected by both N_2 - N_2 and O_2 - O_2 collision-induced continua (cf. the last term in Eq. (8)) [25,26,30].

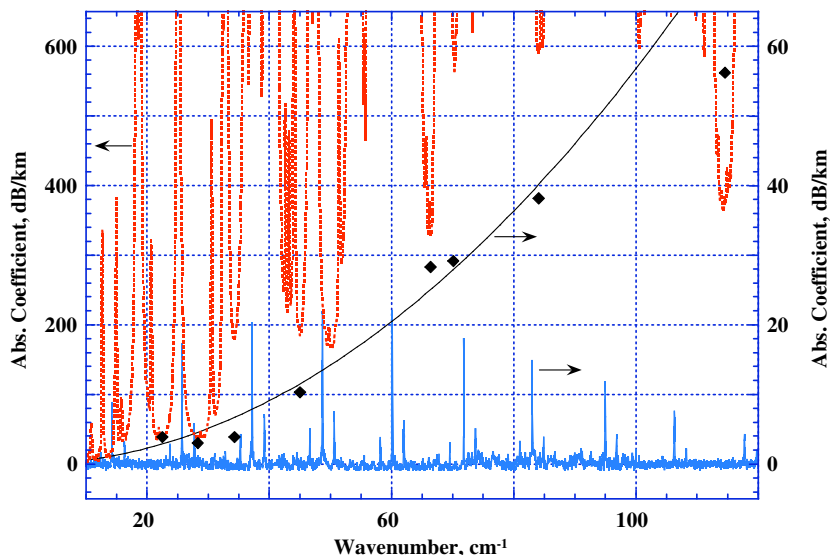


Fig. 3. Absorption components of the H₂O–O₂ mixture at 294 K. The dotted curve spectrum presents a resonance absorbance of a mixture of 1.36 kPa of H₂O and 79.2 kPa of O₂, left absorbance scale. The diamonds and solid fitting curve are related to the H₂O–O₂ continuum as in Fig. 1a. The bottom spectrum demonstrates the absorption of pure oxygen at $P = 79.2$ kPa, absorbance scale is on the right.

5. Conclusions

In this work, we presented new experimental measurements and theoretical calculations for the H₂O–O₂ continuum in the THz spectral region. The measurements were made at 5 temperatures (from 294 to 333 K) in 9 micro-windows ranging from 22.5 to 114.6 cm^{−1}. Given the uncertainties, the agreement is good over the entire frequency and temperature ranges. Unlike our previous work on the continuum for H₂O–N₂ [21], one has an additional absorption component due to the magnetic dipole absorption of O₂. Therefore, we measured the spectrum of pure O₂ over the entire range up to 120 cm^{−1}. If one excludes the data for the 114.6 cm^{−1} micro-window where the ν^2 dependence was not justified, our final results for the absorption coefficient are 0.066(300/ T)^{4.7} (dB/km)/(kPa THz)². As expected this is smaller than the values found for H₂O–N₂ (0.185(300/ T)^{5.7} (dB/km)/(kPa THz)² in Ref. [21]) with a slightly smaller T dependence. Together with the experimental data for the ν^2 -fitted self-continuum [20,21] (3.83(300/ T)^{8.8} (dB/km)/(kPa THz)² in Ref. [21]), the full set of absorption coefficients and temperature exponents may be used for calculations of continuum for H₂O–air in the range between 22.5 and 84.1 cm^{−1} over different temperatures. These calculations can then be compared with other data, for instance those inferred from actual atmospheric measurements [30]. From the above results for the THz micro-windows, one can see a quite complicated dependence of total absorption on gas composition, humidity and temperature.

Acknowledgments

The authors from NIST acknowledge with thanks support from the Upper Atmospheric Research Program of NASA, Grant NNH05A-B211. Ma and Tipping acknowledge financial support from NASA under Grants NAG5-13337, NNG06GB23G, and FCCS-547. The authors would like to thank the National Energy Research Scientific Computing Center (Livermore, CA) for computer time and facilities provided.

Appendix

The explicit expression for the induced interaction potential for the H₂O–O₂ pair (or the H₂O–N₂ pair) is given by

$$V_{\text{ind}}(r, \Omega_a, \Omega_b) = -\frac{1}{2} \left(\alpha_{(\text{O}_2)} - \frac{\gamma_{(\text{O}_2)}}{3} \right) \left\{ \frac{\mu^2}{r^6} [1 + 3 \cos^2 \beta] + \frac{4\mu}{r^7} [Q_{ca} \cos \beta \sin^2 \beta \cos 2\gamma + 3Q_{bb} \cos^3 \beta] + \frac{1}{r^8} \left[Q_{ca}^2 \sin^2 \beta \left(1 + \frac{5}{4} \sin^2 \beta \cos^2 2\gamma \right) + \frac{9}{4} Q_{bb}^2 (5 \cos^4 \beta - 2 \cos^2 \beta + 1) + \frac{3}{2} Q_{ca} Q_{bb} \sin^2 \beta \cos 2\gamma (5 \cos^2 \beta - 3) \right] \right\} - \frac{\gamma_{(\text{O}_2)}}{2} \left\{ \frac{\mu^2}{r^6} E^2 + \frac{2\mu E}{r^7} (Q_{ca} F + Q_{bb} H) + \frac{1}{8} (Q_{ca} F + Q_{bb} H)^2 \right\},$$

where H₂O is given in the similar representation, $Q_{ca} \equiv Q_{cc} - Q_{aa}$, $\alpha_{(\text{O}_2)}$ and $\gamma_{(\text{O}_2)}$ are the isotropic and anisotropic parts of the polarizability of O₂. In the above expression, E , H , and F are defined by

$$E = C_{12} - 3 \cos \theta \cos \beta, \\ H = 3 \cos \beta C_{12} + \frac{3}{2} \cos \theta (1 - 5 \cos^2 \beta), \\ F = \cos 2\gamma \left[\frac{1}{2} \cos \theta (5 \cos^2 \beta - 3) - \cos \beta C_{12} \right] + \sin 2\gamma \sin \theta \sin \beta \sin(\alpha - \phi),$$

where

$$C_{12} = \cos \theta \cos \beta + \sin \theta \sin \beta \cos(\alpha - \phi).$$

References

- [1] A. Deepak, T.D. Wilkerson, L.H. Ruhnke (Eds.), *Atmospheric Water Vapor*, Academic Press, New York, 1980.
- [2] D.E. Burch, D.A. Gryvnak, F.J. Gates, Final Report AFCRL-TR-74-0377, Hanscom AFB, MA, 1974.
- [3] D.E. Burch, R.L. Alt, Air Force Geophys., Lab Report AFGL-TR-84-0128, Hanscom AFB, MA, 1984.
- [4] M.T. Coffee, Quart. J.R. Met. Soc. 103 (1977) 685–692.
- [5] J. Hinderling, M.W. Sigrist, F.K. Kneubuhl, *Infrared Phys.* 27 (1987) 63–120.
- [6] D.E. Burch, *JOSA* 58 (1968) 383–394.
- [7] P.W. Rosenkranz, *J. Chem. Phys.* 83 (1985) 6139–6144.
- [8] P.W. Rosenkranz, *Chem. Phys.* 87 (1987) 163–170.
- [9] Q. Ma, R.H. Tipping, *J. Chem. Phys.* 93 (1990) 7066–7075.

- [10] Q. Ma, R.H. Tipping, *J. Chem. Phys.* 95 (1991) 6290–6301;
Q. Ma, R.H. Tipping, *J. Chem. Phys.* 96 (1992) 8655–8663;
Q. Ma, R.H. Tipping, *J. Chem. Phys.* 97 (1992) 818–828.
- [11] Q. Ma, R.H. Tipping, *J. Chem. Phys.* 111 (1999) 5909–5921.
- [12] Q. Ma, R.H. Tipping, *J. Chem. Phys.* 112 (2000) 574–584.
- [13] Q. Ma, R.H. Tipping, *J. Chem. Phys.* 93 (1990) 6127–6139.
- [14] H.J. Liebe, *Intl. J. Infrared Millimeter Waves* 10 (1989) 631–650.
- [15] Q. Ma, R.H. Tipping, *J. Chem. Phys.* 117 (2002) 10581–10596.
- [16] A. Bauer, M. Godon, *J. Quant. Spectrosc. Radiat. Transf.* 46 (1991) 211–220.
- [17] A. Bauer, M. Godon, J. Carlier, Q. Ma, R.H. Tipping, *J. Quant. Spectrosc. Radiat. Transf.* 50 (1993) 463–475.
- [18] A. Bauer, M. Godon, J. Carlier, Q. Ma, *J. Quant. Spectrosc. Radiat. Transf.* 53 (1995) 411–423.
- [19] A.I. Meshkov, Ph.D. Dissertation, The Ohio State University, 2006.
- [20] V.B. Podobedov, D.F. Plusquellic, G.T. Fraser, *J. Quant. Spectrosc. Radiat. Transf.* 91 (2005) 287–295.
- [21] V.B. Podobedov, D.F. Plusquellic, K.M. Siegrist, G.T. Fraser, Q. Ma, R.H. Tipping, *J. Quant. Spectrosc. Radiat. Transf.* 109 (2008) 458–467.
- [22] H.J. Liebe, P.W. Rosenkranz, G.A. Hufford, *J. Quant. Spectrosc. Radiat. Transf.* 48 (1992) 629–643.
- [23] Numerical Recipes in Fortran 77, in: W.H. Press, S.A. Teukolsky, W.T. Vetterling, B.P. Flannery (Eds.), Cambridge University Press, Cambridge, 1992.
- [24] J. Verhoeven, A. Dymanus, *J. Chem. Phys.* 52 (1970) 3222–3233.
- [25] G. Moreau, J. Boisssoles, C. Boulet, R.H. Tipping, Q. Ma, *J. Quant. Spectrosc. Radiat. Transf.* 64 (2000) 87–107.
- [26] J. Boisssoles, R.H. Tipping, C. Boulet, *J. Quant. Spectrosc. Radiat. Transf.* 51 (1994) 615–627.
- [27] D.F. Plusquellic, R.D. Suenram, B. Mate, J.O. Jensen, A.C. Samuels, *J. Chem. Phys.* 115 (2001) 3057–3067.
- [28] J.H. Van Vleck, V.F. Weisskopf, *Rev. Mod. Phys.* 17 (1945) 227–236.
- [29] Y. Scribano, C. Leforestier, *J. Chem. Phys.* 126 (2007) 234301–234312.
- [30] J.R. Pardo, E. Serabyn, J. Cernicharo, *J. Quant. Spectrosc. Radiat. Transf.* 68 (2001) 419–433.
- [31] M.A. Koshelev, M.Yu. Tretyakov, G.Yu. Golubiatnicov, V.V. Parshin, V.N. Markov, L.A. Koval, *J. Mol. Spectrosc.* 241 (2007) 101–108.
- [32] P.W. Rosenkranz, *Radio Sci.* 33 (1998) 919–928.
- [33] J.W. Waters, *Methods Exp. Phys.* 12B (1976) 142–176.
- [34] S.A. Clough, F.X. Kneizys, R.W. Davies, *J. Atmos. Res.* 23 (1989) 229–241.
- [35] H.A. Gebbie, W.J. Burroughs, G.R. Bird, *Proc. Roy. Soc. A* 310 (1969) 579–590.
- [36] Yu.P. Kalmykov, S.V. Titov, *Izv. Vyssh. Uch. Zaved. Radiophysica* 32 (1988) 933–944.